Journal of Materials Science: Materials in Electronics (2018) 29:8020–8030
https://doi.org/10.1007/s10854-018-8808-7

Al^{3+} doped M-type hexagonal Ba–Co ferrites synthesized via ball-milling assisted ceramic process: magnetism and its correlation with structural properties

Wen Chen[1] · Wenwei Wu[1,2] · Miaoyu Li[1] · Chong Zhou[1] · Shifang Zhou[1]

Received: 15 September 2017 / Accepted: 22 February 2018 / Published online: 23 February 2018

Abstract

$Ba_{0.5}Co_{0.5}Al_xFe_{12-x}O_{19}$ ($x = 0$, 0.08, 0.16, and 0.24) hexaferrites are synthesized via ball-milling assisted ceramic process, and their crystal structure, microstructure, and magnetic properties were studied. The results show that all samples, calcined between 950 and 1150 °C, consist of the main M-type hexagonal Ba ferrite phase in combination of a small amount of $CoFe_2O_4$ and Fe_2O_3 phase. The lattice parameters of M-type hexagonal $Ba_{0.5}Co_{0.5}Al_xFe_{12-x}O_{19}$ decrease after Al^{3+} doping. The addition of Al^{3+} ions results in a reduction of crystallite size, which is attributed that the presence of foreign phase $CoFe_2O_4$ and Fe_2O_3 restrains the growth of the $Ba_{0.5}Co_{0.5}Al_xFe_{12-x}O_{19}$ crystallite. Magnetic characterization indicates that all samples exhibit hard magnetic properties. Trend of specific saturation magnetization of $Ba_{0.5}Co_{0.5}Al_xFe_{12-x}O_{19}$ sample, calcined at 1050 and 1150 °C, decreases with the increase in Al^{3+} content. The varied magnetic properties with substitution content (x) are well explained by the occupancy effects of Al^{3+} ions in magnetoplumbite structure. $Ba_{0.5}Co_{0.5}Fe_{12}O_{19}$, calcined at 1150 °C, has the highest specific saturation magnetization value (56.07 emu/g), remanence (28.66 emu/g), and moment (10.76 μ_B). Besides, with the increase of substitution content (x), magnetic domain type of ferrites, calcined at 1150 °C, changes from a single magnetic domain to a multi-domain type.

1 Introduction

Barium hexaferrite ($BaFe_{12}O_{19}$) is a well-known permanent magnet with relatively high Curie temperature ($T_C = 502$ °C) [1, 2] and specific saturation magnetization [3], high values for melting point (1390 °C) [4], coercivity [5], and magnetic anisotropy [6, 7], as well as excellent chemical stability and corrosion resistivity [8]. Barium hexaferrite has been extensively used as permanent magnets, microwave devices and magnetic recording media. The magnetic properties of the hexaferrites particles used in electronic and recording media depend highly on the crystallite size, shape, purity, and magnetic stability. These particles should have following conditions, including single-domain structure, high coercivity and relatively high specific saturation magnetization [8]. In the hexagonal $BaFe_{12}O_{19}$ ferrite, the Fe^{3+} ions are distributed over five different sites: three octahedral sites (12k, $4f_2$ and 2a), one tetrahedral site ($4f_1$), and one bipyramidal site (2b). The sites of 12k, 2a, and 2b have upward spin direction, while the $4f_1$ and $4f_2$ sites have downward spin directions. The magnetic moment (M) of each molecule hexagonal $BaFe_{12}O_{19}$ ferrite can be written as the following equation [9, 10]: $\vec{M} = \vec{2a} + \vec{2b} + \vec{12k} + \vec{4f_1} + \vec{4f_2}$. Therefore, magnetic properties of barium hexaferrite can be tailored by distribution of different cations at octahedral, tetrahedral, and bipyramidal sites. To date, some studies have been carried out. For example, Ba^{2+} ions were substituted by rare earth ions or alkaline-earth metals (such as Ho^{3+}, Ce^{3+}, La^{3+}, Pr^{3+}, Sm^{3+}, Ca^{2+}, etc) [11–15]; Fe^{3+} ions are substituted by different cations (such as Nd^{3+}, Co^{2+} or Co^{3+}, Al^{3+}, Ni^{2+}, etc) [16–19], and the hexagonal Ba ferrites underwent combined substitution (such as, Sr–Pr, Co–Zn–Sn, Co–Al, Zn–Co–Zr, Mn–Sn, etc) [20–24]. Magnetic properties of these materials depend mostly on their composition, grain size, and phase purity. For example, Mosleh et al. [12] synthesized M-type hexagonal $Ba_{1-x}Ce_xFe_{12}O_{19}$ ($x = 0.0$, 0.05, 0.1, 0.15, and 0.2) polycrystalline samples by the sol–gel

✉ Wenwei Wu
gxuwuwenwei@aliyun.com; wuwenwei@gxu.edu.cn

[1] School of Chemistry and Chemical Engineering, Guangxi University, Nanning 530004, People's Republic of China

[2] Guangxi Colleges and Universities Key Laboratory of Applied Chemistry Technology and Resource Development, Nanning 530004, People's Republic of China

method, followed by sintering in air at 1100 °C for 3 h. Maximum values of magnetization (53 emu/g) and coercivity (5088 Oe) were obtained for substitution content of $x = 0.1$. Teh et al. [17] synthesized $BaM_xFe_{12-x}O_{19}$ [$x = 1.0$, M = Co(II) or Co(III)] by the sol–gel method, followed by calcining in air at a temperature of 800(± 10) °C for 3 days with intermediate grindings. Specific saturation magnetizations of $BaFe_{12}O_{19}$, $BaFe_{11}Co(II)O_{19-\delta}$, and $BaFe_{11}Co(III)O_{19}$ are 47.8, 27.8, and 50.4 emu/g, respectively. Dhage et al. [18] synthesized $BaFe_{12-x}Al_xO_{19}$ ($x = 0.00$, 0.25, 0.50, 0.75, 1.00) by the solution combustion technique, followed by sintering in air at 900 °C for 8 h. Pure barium hexaferrite shows only single phase hexagonal structure while samples with $0.25 \le x \le 1.00$ substitution content consist of the main M-phase barium hexaferrite in combination of a small amount of α-Fe_2O_3. The specific saturation magnetization (Ms) and magneton number (n_B) decrease from 38.57 to 21.73 emu/g and from 7.675 to 4.213 μ_B, respectively, with the increase in substitution content from $x = 0.0$ to 1.0. Alam et al. [23] synthesized M-type $BaZn_xCo_xZr_{2x}Fe_{12-4x}O_{19}$ ($x = 0.0$, 0.1, 0.2, 0.3, 0.4, and 0.5) nanoparticles by the co-precipitation method in the presence of polyvinyl alcohol (PVA), followed by sintering in air at 950 °C for 2 h. The results show that the specific saturation magnetization and coercivity decrease from 84.53 to 52.81 emu/g, 3750 to 440 Oe, respectively, as substitution content increases from $x = 0$ to $x = 0.5$. However, as far as we know, there is no report available for structure, lattice strain, and magnetic properties of $Ba_{0.5}Co_{0.5}Al_xFe_{12-x}O_{19}$ ($x = 0$, 0.08, 0.16, and 0.24) synthesized by the ball-milling, followed by calcination in air using $BaC_2O_4{\cdot}2H_2O$, $CoC_2O_4{\cdot}2H_2O$, $Al(OH)_3$, and $FeC_2O_4{\cdot}2H_2O$ as raw materials.

In this paper, the hexaferrite $Ba_{0.5}Co_{0.5}Al_xFe_{12-x}O_{19}$ ($x = 0$, 0.08, 0.16, and 0.24) magnetic powders were synthesized by the ball-milling assisted ceramic process. The structure, lattice strain, and magnetic properties of the samples have been investigated systematically.

2 Experimental procedures

All samples of M-type hexagonal ferrites $Ba_{0.5}Co_{0.5}Al_xFe_{12-x}O_{19}$ ($x = 0$, 0.08, 0.16, and 0.24) were synthesized by ball-milling assisted ceramic process [25]. The raw materials used in this study were $BaC_2O_4{\cdot}2H_2O$, $CoC_2O_4{\cdot}2H_2O$, $Al(OH)_3$, and $FeC_2O_4{\cdot}2H_2O$ of analytical grade. In a typical synthesis ($Ba_{0.5}Co_{0.5}Fe_{12}O_{19}$), 0.609 g $BaC_2O_4{\cdot}2H_2O$, 0.427 g $CoC_2O_4{\cdot}2H_2O$, 10.066 g $FeC_2O_4{\cdot}2H_2O$, and 10 ml ethanol were added to stainless steel ball milling tank of 100 ml. The mixtures of raw materials were milled for 30 min with an angular velocity of 350 rpm and a ball-to-powder weight ratio of about 15:1. The $Ba_{0.5}Co_{0.5}Fe_{12}O_{19}$ precursor was obtained after drying the mixture in air at 80 °C for 5 h. A similar synthesis procedure was used to synthesize other $Ba_{0.5}Co_{0.5}Al_xFe_{12-x}O_{19}$ precursor. Finally, the precursor powder was calcined at 950, 1050, and 1150 °C for 3 h, respectively, at a heating rate of 2 °C/min in air to produce M-type hexagonal $Ba_{0.5}Co_{0.5}Al_xFe_{12-x}O_{19}$.

The TG/DSC measurements were conducted using a Netzsch Sta 409 PC/PG thermogravimetric analyzer under continuous flow of air (30 ml/min). The sample mass was 9.55 mg. The phase purity of the studied hexaferrites was carried out using a X′pert PRO X-ray diffractometer (XRD), using Cu Kα radiation ($\lambda = 0.15406$ nm) at room temperature in the range of 5–75°. The micromorphology of the samples was investigated using a S-3400 scanning electron microscope (SEM). The Fourier transform infrared spectra (FT-IR) spectra of the calcined samples were recorded on a Nexus 470 Fourier transform IR instrument. Magnetic measurements were done using a vibrating sample magnetometer (VSM, Lake Shore 7410) at room temperature and under an applied magnetic field up to 20 kOe. Magnetic parameters, including the specific saturation magnetization (Ms), remanence (Mr), and coercivity (Hc), were calculated from the hysteresis loops of samples.

3 Results and discussion

3.1 Composition analysis of the precursor

0.031 g precursor sample was dissolved in 10 ml 50 vol% HCl solution, and then diluted to 100.00 ml with deionized water. Barium (Ba), cobalt (Co), aluminum (Al), and ferrum (Fe) in the solution were determined by inductively coupled plasma atomic emission spectrometry (ICP-AES, Perkin Elmer Optima 5300 DV). The results were showed in Table 1. Atom ratios of Ba, Co, Al, and Fe in the precursor agreed with those of $Ba_{0.5}Co_{0.5}Al_xFe_{12-x}O_{19}$ ($x = 0$, 0.08, 0.16, and 0.24). For example, $Ba_{0.5}Co_{0.5}Fe_{12}O_{19}$ precursor was determined to be $0.5BaC_2O_4$–$0.5CoC_2O_4$–$12FeC_2O_4{\cdot}14H_2O$.

Table 1 Composition analysis of $Ba_{0.5}Co_{0.5}Al_xFe_{12-x}O_{19}$ precursor

Composition, x	Mass percentage (%)				Atom ratio (Ba:Co:Fe:Al)
	Ba	Co	Fe	Al	
0.0	3.172	1.361	30.980	0.000	0.50:0.50:12.01:0.00
0.08	3.179	1.365	30.826	0.100	0.50:0.50:11.92:0.08
0.16	3.192	1.370	30.735	0.201	0.50:0.50:11.84:0.16
0.24	3.203	1.375	30.638	0.302	0.50:0.50:11.76:0.24

3.2 TG/DSC analysis of the precursor

Figure 1 shows the TG/DSC curves of the $Ba_{0.5}Co_{0.5}Fe_{12}O_{19}$ precursor at a heating rate of 10 °C/min. The TG/DSC curves show that the thermal transformation of $0.5BaC_2O_4$–$0.5CoC_2O_4$–$12FeC_2O_4{\cdot}14H_2O$ below 1200 °C occurred in three well-defined steps. The first step started at about 153.6 °C and ended at 194.3 °C, and is characterized by a weak endothermic DSC peak at 190.6 °C, which can be attributed to the dehydration of 14 molecules of water from $0.5BaC_2O_4$–$0.5CoC_2O_4$–$12FeC_2O_4{\cdot}14H_2O$ (mass loss: observed, 11.15%; theoretical, 11.65%). The second transformation step started at 194.3 °C and ended at 257.8 °C, and is characterized by a strong exothermic DSC peak at 225.8 °C, attributed to the reaction of $0.5CoC_2O_4$–$12FeC_2O_4$ with $9.25O_2$ into $0.5CoO$, $6Fe_2O_3$, and $25CO_2$ (mass loss: observed, 35.55%; theoretical, 37.15%). The third transformation step started at 257.8 °C and ended at 284.6 °C, attributed to the reaction of $0.5BaC_2O_4$ with $0.25O_2$ into 0.5BaO and CO_2 (mass loss: observed, 1.56%; theoretical, 1.66%). The weak and broad exothermic peak at about 850 °C is attributed to crystallization of hexagonal $Ba_{0.5}Co_{0.5}Fe_{12}O_{19}$.

3.3 XRD and SEM analyses of the calcined products

Figure 2 represents X-ray diffraction patterns of $Ba_{0.5}Co_{0.5}Al_xFe_{12-x}O_{19}$ ($x=0$, 0.08, 0.16, and 0.24) ferrite samples calcined at different temperature for 3 h. The XRD patterns were indexed to be hexagonal magnetoplumbite (M-type) crystal structure having space group P63/mmc(194) (JCPDS no. 43-0002). The XRD analysis of all samples, calcined at different calcination temperature, confirm the formation of M-type hexagonal Ba ferrite in combination of a small amount of $CoFe_2O_4$ and Fe_2O_3 phase.

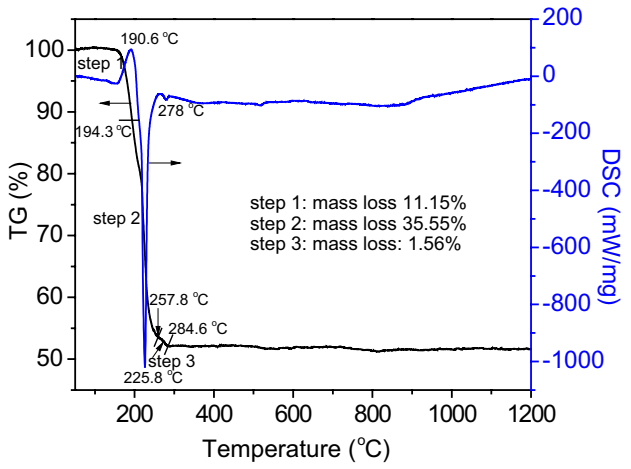

Fig. 1 TG/DSC curves of the $0.5BaC_2O_4$–$0.5CoC_2O_4$–$12FeC_2O_4{\cdot}14H_2O$ at a heating rate of 10 °C/min in air

The presence of Fe_2O_3 and $CoFe_2O_4$ can be related to a higher disorder in the $BaFe_{12}O_{19}$ structure due to higher Co content. The substitutions of Al^{3+} ions for Fe^{3+} ions do not change the M-type hexagonal ferrite crystalline structure of $MFe_{12}O_{19}$ except that the diffraction peaks shift slightly to a lower degree at $x=0.08$, then to higher degree with the increase in Al^{3+} content (Fig. 2e).

The lattice constants a and c values of the hexaferrites $Ba_{0.5}Co_{0.5}Al_xFe_{12-x}O_{19}$ are calculated from the values of the d_{hkl} corresponding to (107) peaks and (114) peaks using the following Eq. (1) [26] and the results are listed in Table 2.

$$d_{hkl} = \left(\frac{4}{3} \times \frac{h^2 + hk + k^2}{a^2} + \frac{l^2}{c^2}\right)^{-1/2}, \quad (1)$$

The value of 'a' and 'c' slightly decreases with increasing substitution content (x). This may be due to the smaller Al^{3+} ions (0.051 nm) [27] which simply substitute the larger Fe^{3+} ions (0.067 nm) [28] without distortion of the hexagonal symmetry of the host Ba–Co hexaferrite. Similar results are also reported for M-type hexagonal $BaAl_xFe_{12-x}O_{19}$ ferrites by Chen et al. [29], and M-type hexagonal $SrAl_xFe_{12-x}O_{19}$ by Wang et al. [30].

The crystallinity of $Ba_{0.5}Co_{0.5}Al_xFe_{12-x}O_{19}$ is estimated using Eq. (2) or Eq. (3) [31, 32].

$$\text{Crystallinity}(\%) = \frac{I_{\text{peaks of } BaFe_{12}O_{19}}}{I_{\text{all peaks}}}, \quad (2)$$

or

$$\text{Crystallinity}(\%) = \frac{A_{\text{peaks of } BaFe_{12}O_{19}}}{A_{\text{all peaks}}}, \quad (3)$$

where I and A are the intensity and the area of the XRD peaks, respectively. The crystallinity of $Ba_{0.5}Co_{0.5}Al_xFe_{12-x}O_{19}$ ($x=0$, 0.08, 0.16, and 0.24), obtained at different temperatures, is shown in Fig. 3. The crystallinity of $Ba_{0.5}Co_{0.5}Al_xFe_{12-x}O_{19}$ increases with the increase in calcination temperature except for $Ba_{0.5}Co_{0.5}Al_{0.08}Fe_{11.92}O_{19}$. Besides, the crystallinity of $Ba_{0.5}Co_{0.5}Al_xFe_{12-x}O_{19}$, calcined at 1150 °C, decreases with the increase in substitution content (x). The crystallinities of $Ba_{0.5}Co_{0.5}Al_xFe_{12-x}O_{19}$, obtained at 1150 °C, are 69.20% for $x=0$, 67.27% for $x=0.08$, 65.50% for $x=0.16$, and 65.08% for $x=0.24$, respectively.

The crystallite size is calculated by using the Scherrer formula [33] given by Eq. (4).

$$D = K\lambda/(\beta \cos\theta), \quad (4)$$

where D is the crystallite size, K the Scherrer constant equal to 0.89, λ the wave length (0.15406 nm), θ the corresponding angle, and β the full width at half maxima, The instrumental

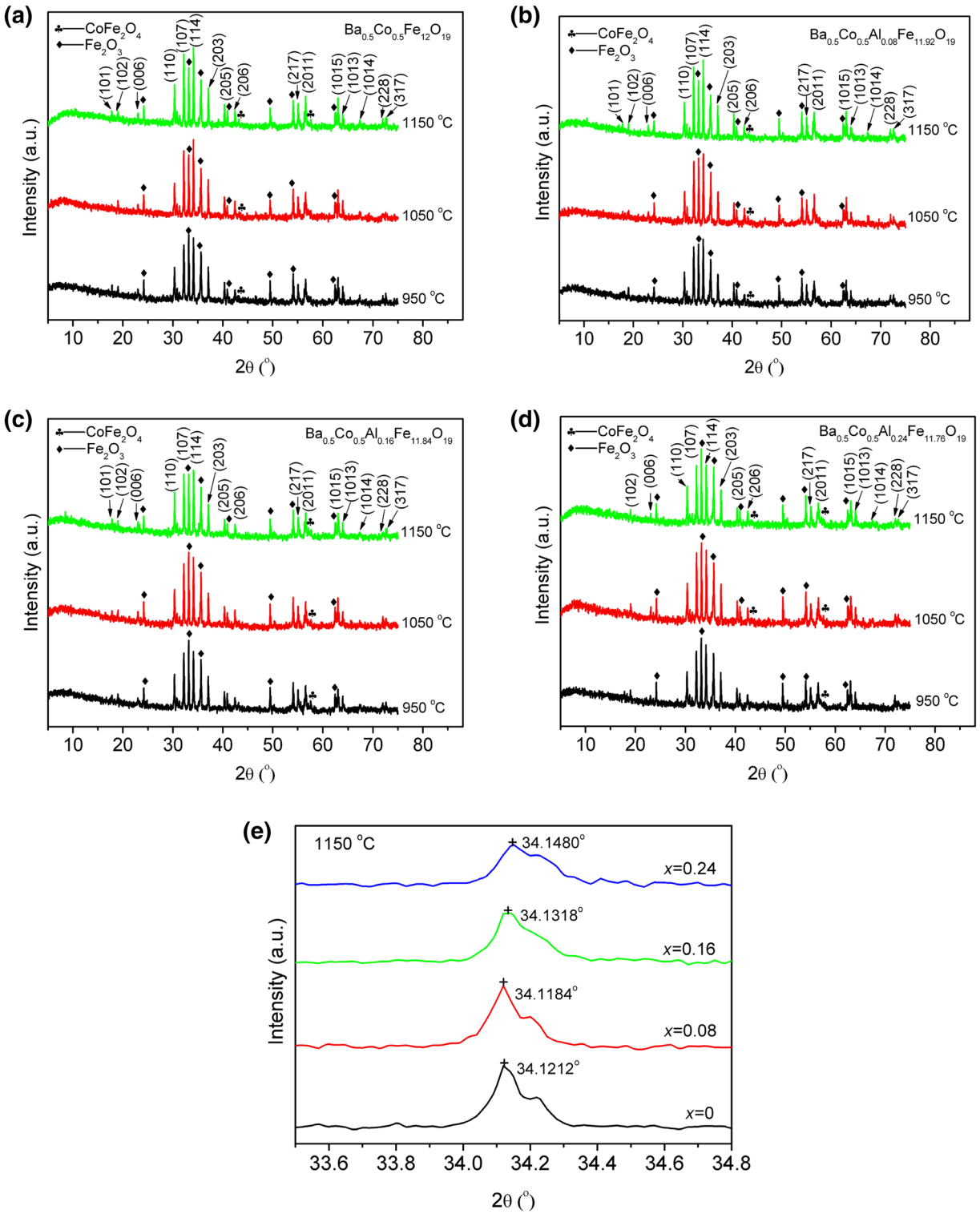

Fig. 2 XRD patterns of $Ba_{0.5}Co_{0.5}Al_xFe_{12-x}O_{19}$: **a** $Ba_{0.5}Co_{0.5}Fe_{12}O_{19}$, **b** $Ba_{0.5}Co_{0.5}Al_{0.08}Fe_{11.92}O_{19}$, **c** $Ba_{0.5}Co_{0.5}Al_{0.16}Fe_{11.84}O_{19}$, **d** $Ba_{0.5}Co_{0.5}Al_{0.24}Fe_{11.76}O_{19}$, and **e** local magnification

Table 2 Structural properties of $Ba_{0.5}Co_{0.5}Al_xFe_{12-x}O_{19}$ calcined at 1150 °C

Composition (x)	a (nm)	c (nm)	c/a	Lattice strains (%)	d_{114} (nm)
0.0	0.58870 (7)	2.31848 (5)	3.9383	0.1293 (5)	0.2625 (6)
0.08	0.58892 (2)	2.31902 (1)	3.9377	0.1379 (0)	0.2625 (8)
0.16	0.58874 (4)	2.31880 (3)	3.9386	0.1336 (3)	0.2624 (8)
0.24	0.58849 (7)	2.31729 (6)	3.9377	0.1719 (5)	0.2623 (6)

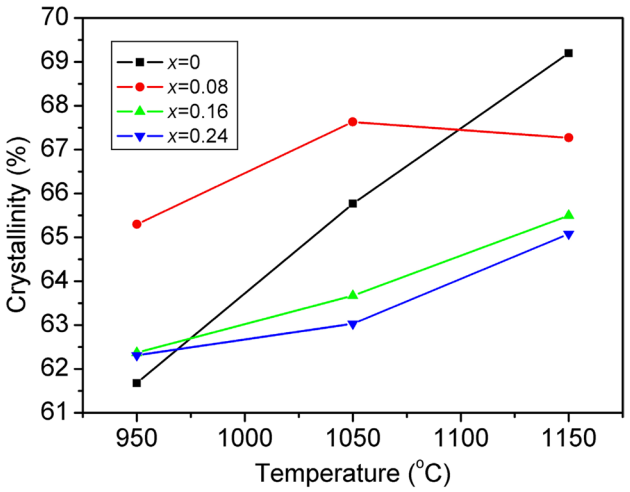

Fig. 3 Dependence of crystallinity of $Ba_{0.5}Co_{0.5}Al_xFe_{12-x}O_{19}$ on calcination temperature and Al^{3+} content

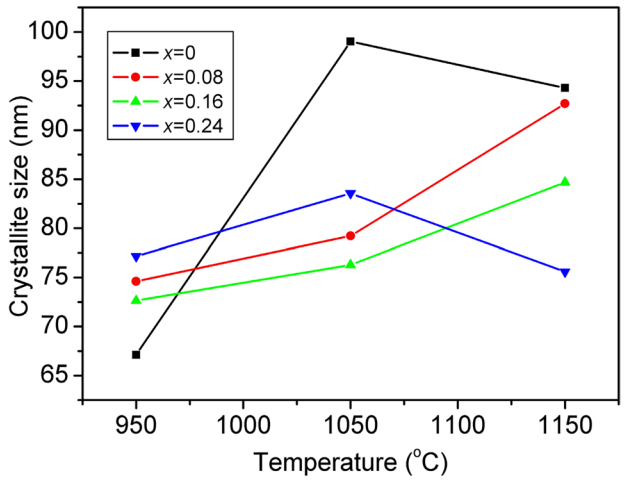

Fig. 4 Dependence of crystallite size of $Ba_{0.5}Co_{0.5}Al_xFe_{12-x}O_{19}$ on calcination temperature and Al^{3+} content

broadening factor has been considered during the FWHM calculation. That is, $\beta = \sqrt{\beta_{obs}^2 - \beta_{ins}^2}$.

The $d_{(114)}$ interplanar spacing of $Ba_{0.5}Co_{0.5}Al_xFe_{12-x}O_{19}$ is calculated by the following Bragg equation [25].

$$d_{(1\,1\,4)} = \frac{\lambda}{2\sin\theta_{(1\,1\,4)}}, \tag{5}$$

The crystallite size (D) of $Ba_{0.5}Co_{0.5}Al_xFe_{12-x}O_{19}$, obtained at different temperatures and $d_{(114)}$ interplanar spacing of $Ba_{0.5}Co_{0.5}Al_xFe_{12-x}O_{19}$, calcined at 1150 °C, are shown in Fig. 4 and Table 2, respectively. From Fig. 4, crystallite size of $Ba_{0.5}Co_{0.5}Al_xFe_{12-x}O_{19}$ ($x = 0.08$, 0.16) increases with the increase in calcination temperature. Besides, the crystallite size of $Ba_{0.5}Co_{0.5}Al_xFe_{12-x}O_{19}$ sample, calcined at 1150 °C, decreases obviously after substituting by Al^{3+} ions. The decrease of average crystallite size of $Ba_{0.5}Co_{0.5}Al_xFe_{12-x}O_{19}$ after substituting Fe^{3+} ions by Al^{3+} ions can be explained as follows: The ionic radius of Al^{3+} ion (0.051 nm) [27] is smaller than that of Fe^{3+} ion (0.067 nm) [28]. In other words, the bond energy of Al^{3+}–O^{2-} is larger than that of Fe^{3+}–O^{2-}. When Al^{3+} ions enter the hexaferrites lattice to form Al^{3+}–O^{2-} bonds, the crystal nucleation and growth of Al^{3+} substituted $Ba_{0.5}Co_{0.5}Fe_{12}O_{19}$ will consume more energy, resulting in the decreases of average crystallite size after substituting Fe^{3+} ions by Al^{3+} ions [34]. On the other hand, the crystallinity of $Ba_{0.5}Co_{0.5}Al_xFe_{12-x}O_{19}$ decreases with the increase in Al^{3+} content. The presence of foreign phase $CoFe_2O_4$ and Fe_2O_3 restrains the growth of the $Ba_{0.5}Co_{0.5}Al_xFe_{12-x}O_{19}$ crystallite. Similar phenomenon was also observed for Al^{3+}-doped $BaFe_{12}O_{19}$ prepared by the solid state reaction method [35]. The $d_{(114)}$ values of the samples in Table 2 reveal that the interplanar spacing decreases with the increase in substitution content (x), which is attributed that ionic radius of Al^{3+} ion (0.051 nm) [27] is smaller than that of Fe^{3+} ion (0.067 nm) [28]. The replacement of Fe^{3+} ions in octahedral sites, tetrahedral site and/or bipyramidal site by Al^{3+} ions would cause the contraction of the unit cell, resulting in smaller $d_{(114)}$ value.

The lattice strains (ε) of the $Ba_{0.5}Co_{0.5}Al_xFe_{12-x}O_{19}$ are estimated using the following Williamson–Hall formula [25]:

$$\varepsilon = \frac{\beta}{4\tan\theta}, \tag{6}$$

where ε is the lattice strain of the structure, β the full width at half maximum (in radian) of the peaks, and θ the corresponding angle of the diffraction peak. Lattice strains of $Ba_{0.5}Co_{0.5}Al_xFe_{12-x}O_{19}$, calcined at 1150 °C, are shown in Table 2. The trend of lattice strains increases with the increase in substitution content (x).

Figure 5 shows the SEM images of the Al^{3+}-substituted Ba–Co ferrite particles calcined at 1050 and 1150 °C for

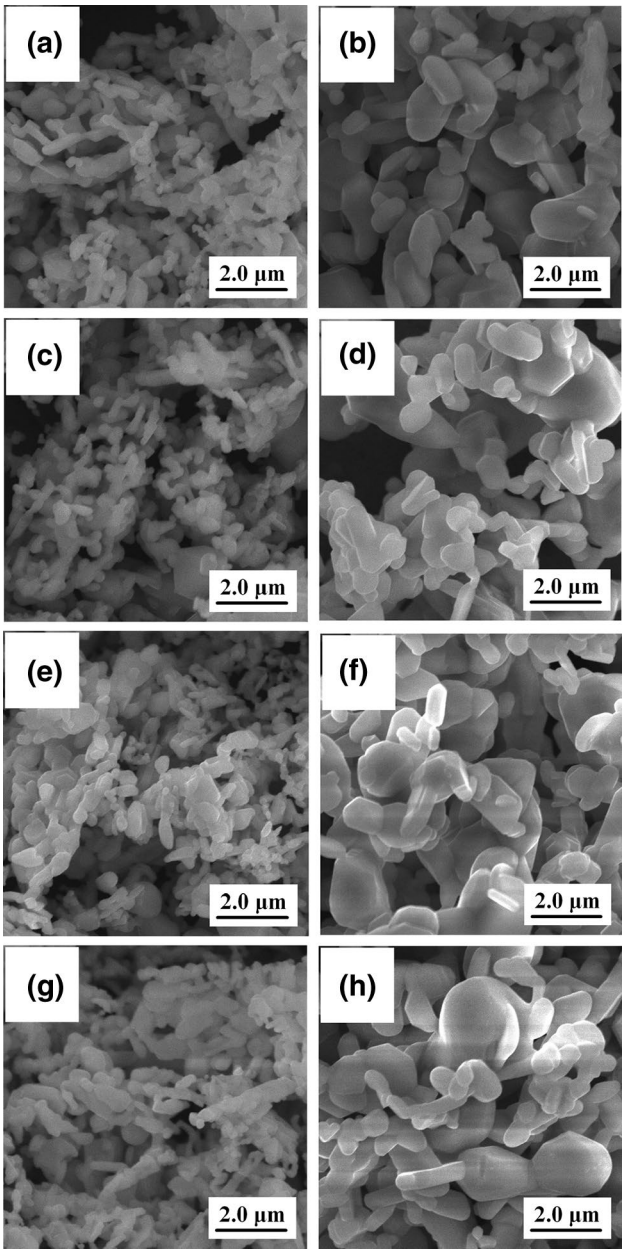

Fig. 5 SEM images of $Ba_{0.5}Co_{0.5}Al_xFe_{12-x}O_{19}$ samples calcined at different temperatures: $Ba_{0.5}Co_{0.5}Fe_{12}O_{19}$ (**a** 1050 °C, **b** 1150 °C), $Ba_{0.5}Co_{0.5}Al_{0.08}Fe_{11.92}O_{19}$ (**c** 1050 °C, **d** 1150 °C), $Ba_{0.5}Co_{0.5}Al_{0.16}Fe_{11.84}O_{19}$ (**e** 1050 °C, **f** 1150 °C), and $Ba_{0.5}Co_{0.5}Al_{0.24}Fe_{11.76}O_{19}$ (**g** 1050 °C, **h** 1150 °C)

3 h. It can be clearly seen that part of the ferrite particles were hexaplatelets, as shown in Fig. 5a–h. Particle size obviously increases with the increase in calcination temperature. The particle size of $Ba_{0.5}Co_{0.5}Al_xFe_{12-x}O_{19}$, calcined at 1050 °C, ranged from 0.25 to 1.5 μm. By contrast, the particle size of the sample, calcined at 1150 °C, ranged from 0.5 to 2.5 μm. In this study, hexagonal platelet-like shape is almost achieved for all the substituted samples, which is a suitable morphology for microwave absorbing [36].

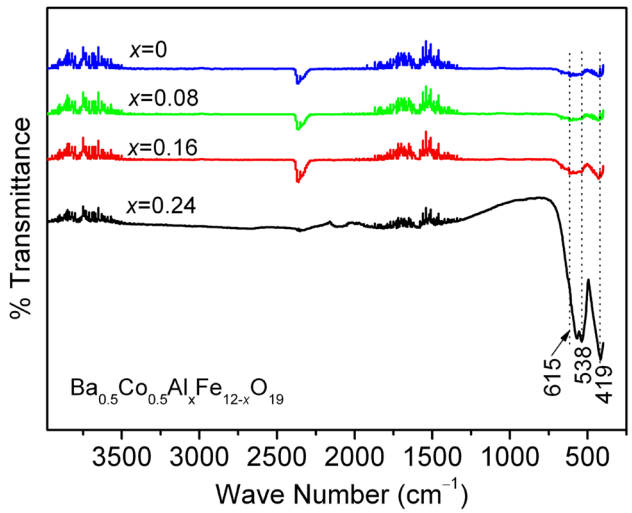

Fig. 6 FT-IR spectra of $Ba_{0.5}Co_{0.5}Al_xFe_{12-x}O_{19}$ calcined at 1150 °C

3.4 FT-IR spectroscopic analysis of $Ba_{0.5}Co_{0.5}Al_xFe_{12-x}O_{19}$

FT-IR spectra of four compositions ($x = 0$, 0.08, 0.16, and 0.24) of $Ba_{0.5}Co_{0.5}Al_xFe_{12-x}O_{19}$ ferrites, calcined at 1150 °C, are shown in Fig. 6. FT-IR spectroscopy explained well the chemical and structural changes of the material. FT-IR spectra of all adsorption bands of the samples are similar, while their relative intensities varied. Band at 419 cm^{-1} is assigned to Fe–O bending vibration by Fe–O_4 and Fe–O stretching mode by Fe–O_6. The band at 538 cm^{-1} is attributed to the Fe–O stretching vibration by Fe–O_4 [9]. The band at about 615 cm^{-1} corresponds to the Ba–O stretching vibration band [9]. After substituting Fe^{3+} ions by Al^{3+} ions, absorption bands of $Ba_{0.5}Co_{0.5}Al_xFe_{12-x}O_{19}$ ($x = 0.08$, 0.16, and 0.24) in the region of 400–730 cm^{-1} become strong with the increase in substitution content (x). Besides, the band at 538 cm^{-1} shift to a higher wave number after substituting Fe^{3+} ions by Al^{3+} ions, which is attributed that the ionic radius of Al^{3+} ion (0.051 nm) [27] is smaller than that of Fe^{3+} ion (0.067) [28]. In other words, the bond energy of Al^{3+}–O^{2-} bond is larger than that of Fe^{3+}–O^{2-}. The band at 615 cm^{-1} shift to a lower wave number after substituting Fe^{3+} ions by Al^{3+} ions, which can be attributed to the substitution of small Al^{3+} ions affecting the distribution of Ba^{2+} ions.

3.5 Magnetic properties of $Ba_{0.5}Co_{0.5}Al_xFe_{12-x}O_{19}$

The *M–H* loops for all Al-substituted samples of composition $Ba_{0.5}Co_{0.5}Al_xFe_{12-x}O_{19}$ ($x = 0$, 0.08, 0.16, and 0.24) magnetic powders were measured up to an applied field of 20 kOe.

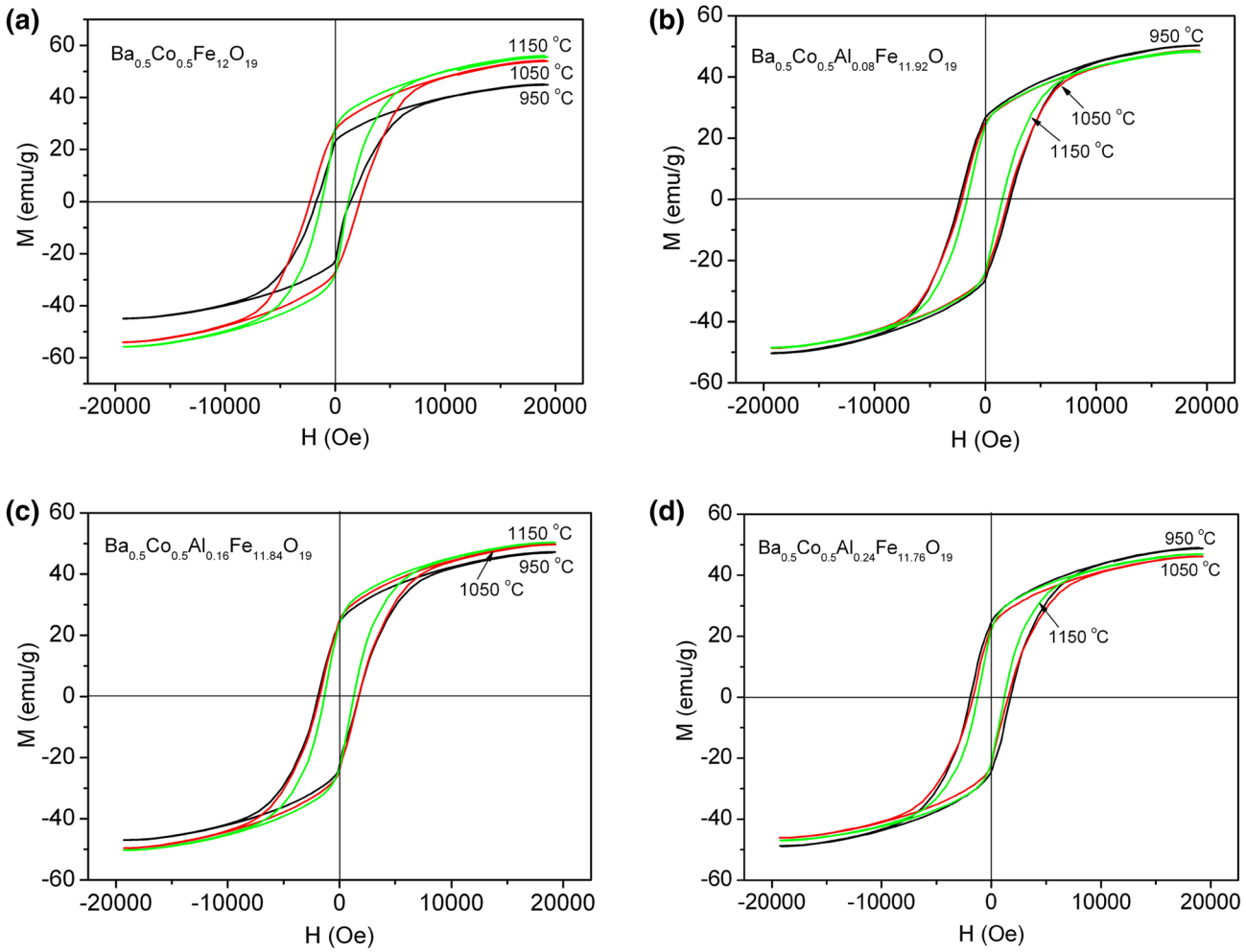

Fig. 7 *M–H* (magnetization–hysteresis) loops of $Ba_{0.5}Co_{0.5}Al_xFe_{12-x}O_{19}$ samples calcined at different temperatures: **a** $Ba_{0.5}Co_{0.5}Fe_{12}O_{19}$, **b** $Ba_{0.5}Co_{0.5}Al_{0.08}Fe_{11.92}O_{19}$, **c** $Ba_{0.5}Co_{0.5}Al_{0.16}Fe_{11.84}O_{19}$, and **d** $Ba_{0.5}Co_{0.5}Al_{0.24}Fe_{11.76}O_{19}$

The results are shown in Fig. 7. From these loops, the values of specific saturation magnetization (*M*s), remanence (*M*r), and coercivity (Hc) for all the samples were obtained. Dependence of specific saturation magnetization and lattice strains of $Ba_{0.5}Co_{0.5}Al_xFe_{12-x}O_{19}$ on substitution content (x) or calcination temperature is shown in Fig. 8. From Fig. 8a, specific saturation magnetization of $Ba_{0.5}Co_{0.5}Fe_{12}O_{19}$ and $Ba_{0.5}Co_{0.5}Al_{0.16}Fe_{11.84}O_{19}$ increases with the increase in calcination temperature; specific saturation magnetization of $Ba_{0.5}Co_{0.5}Al_{0.08}Fe_{11.92}O_{19}$ decreases with the increase in calcination temperature. By contrast, the specific saturation magnetization of $Ba_{0.5}Co_{0.5}Al_{0.24}Fe_{11.76}O_{19}$ decreases with the increase in calcination temperature up to 1050 °C, beyond which it slightly increases. Besides, the trend of specific saturation magnetization of $Ba_{0.5}Co_{0.5}Al_xFe_{12-x}O_{19}$ ($x=0$, 0.08, 0.16, and 0.24), calcined at 1050 and 1150 °C, decreases with the substitution content (x). Similar results are also reported for M-type hexagonal $BaAl_xFe_{12-x}O_{19}$ ferrites prepared via the electrospinning and subsequent heat treatment at 1100 °C for 2 h by Li et al. [37] and M-type hexagonal $Ca_{0.6}Sr_{0.1}La_{0.3}Fe_{12-x}Al_xO_{19}$ prepared via the conventional ceramic techniques by Yang et al. [38]. Specific saturation magnetization evolution of $Ba_{0.5}Co_{0.5}Al_xFe_{12-x}O_{19}$ with Al^{3+} content can be explained as follows: The magnetic moment of per ion for Al^{3+} and Fe^{3+} ions are 0 μ_B and 5 μ_B, respectively. It has been reported that Al^{3+} ions have a preference for substituting Fe^{3+} ions in 2a and 12k sites [37]. So, when the non-magnetic Al^{3+} ions substituted Fe^{3+} ions in $Ba_{0.5}Co_{0.5}Fe_{12}O_{19}$, a minor substitution ($x=0.08$) of Fe^{3+} ions by Al^{3+} ions leads to a rapid decrease of the specific saturation magnetization of Al-substituted samples. In this study, the $Ba_{0.5}Co_{0.5}Fe_{12}O_{19}$, obtained at 1150 and 950 °C, has the highest (56.07 emu/g) and the lowest (45.14 emu/g) specific saturation magnetization values, respectively. The trend of specific saturation magnetization of $Ba_{0.5}Co_{0.5}Al_xFe_{12-x}O_{19}$ decreases with the increase in

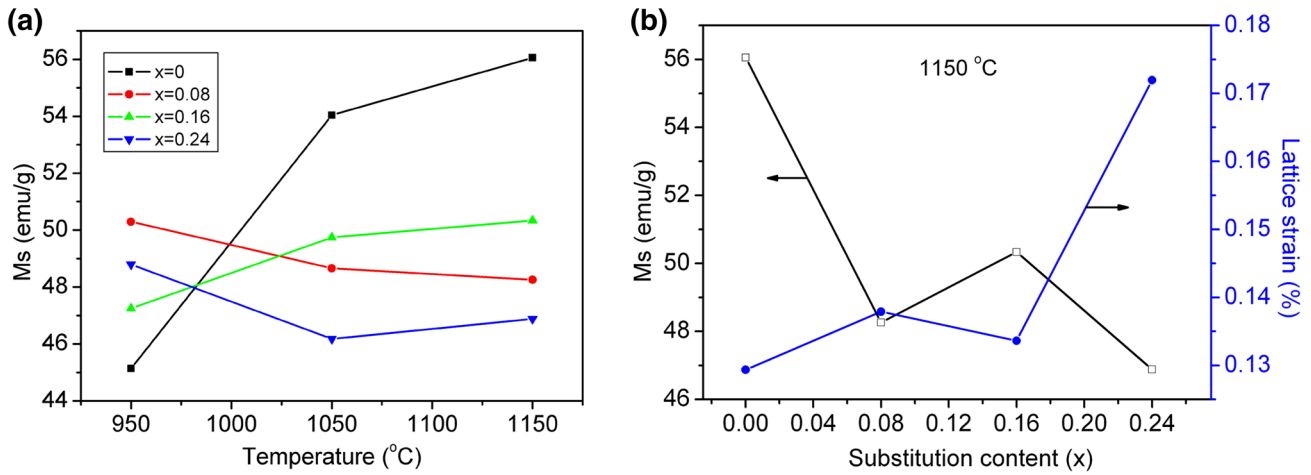

Fig. 8 Dependence of specific saturation magnetization (**a**) and lattice strains (**b**) of $Ba_{0.5}Co_{0.5}Al_xFe_{12-x}O_{19}$ on substitution content (x)

lattice strains (Fig. 7b). This is because that the ionic radius of Al^{3+} ion (0.051 nm) [27] is smaller than that of Fe^{3+} ion (0.067) [28]. Substitution of a minor Al^{3+} ions ($x=0.08$) for Fe^{3+} ions at octahedral sites (12k and 2a) results in the remarkable increase of lattice strains and the decrease of the net magnetic moment for $Ba_{0.5}Co_{0.5}Al_xFe_{12-x}O_{19}$.

Dependence of remanence (Mr) and coercivity (Hc) of $Ba_{0.5}Co_{0.5}Al_xFe_{12-x}O_{19}$ on calcination temperature and substitution content (x) is shown in Fig. 9. From Fig. 9a, remanence of $Ba_{0.5}Co_{0.5}Fe_{12}O_{19}$ increases with the increase in calcination temperature. However, remanence of $Ba_{0.5}Co_{0.5}Al_{0.08}Fe_{11.92}O_{19}$ and $Ba_{0.5}Co_{0.5}Al_{0.24}Fe_{11.76}O_{19}$ decreases with the increase in calcination temperature. By contrast, remanence of $Ba_{0.5}Co_{0.5}Al_{0.16}Fe_{11.84}O_{19}$ increases with the increase in calcination temperature at first, then decreases at 1150 °C. Remanence of $Ba_{0.5}Co_{0.5}Al_xFe_{12-x}O_{19}$ decreases with the increase in substitution content (x). $Ba_{0.5}Co_{0.5}Fe_{12}O_{19}$, calcined at 1150 °C, has the highest remanence value (28.66 emu/g); $Ba_{0.5}Co_{0.5}Al_{0.24}Fe_{11.76}O_{19}$, calcined at 1150 °C, has the lowest remanence value (22.53 emu/g). Coercivity of $Ba_{0.5}Co_{0.5}Fe_{12}O_{19}$ increases with the increase in calcination temperature at first, then decreases at 1150 °C. Coercivity of $Ba_{0.5}Co_{0.5}Al_xFe_{12-x}O_{19}$ ($x=0.08$, 0.16, and 0.24) decreases with the increase in calcination temperature. Besides, coercivity of $Ba_{0.5}Co_{0.5}Al_xFe_{12-x}O_{19}$ ($x=0$, 0.08, 0.16, and 0.24), calcined at 1050 °C, decreases with the increase in substitution content (x). By contrast, coercivity of $Ba_{0.5}Co_{0.5}Al_xFe_{12-x}O_{19}$, calcined at 1150 °C, remarkably increases after a minor of substitution ($x=0.08$). Coercivity evolution of $Ba_{0.5}Co_{0.5}Al_xFe_{12-x}O_{19}$, calcined at 1150 °C, can be explained as follows: crystallite size decreases after doping Al^{3+} ions, and coercivity is inversely proportional to

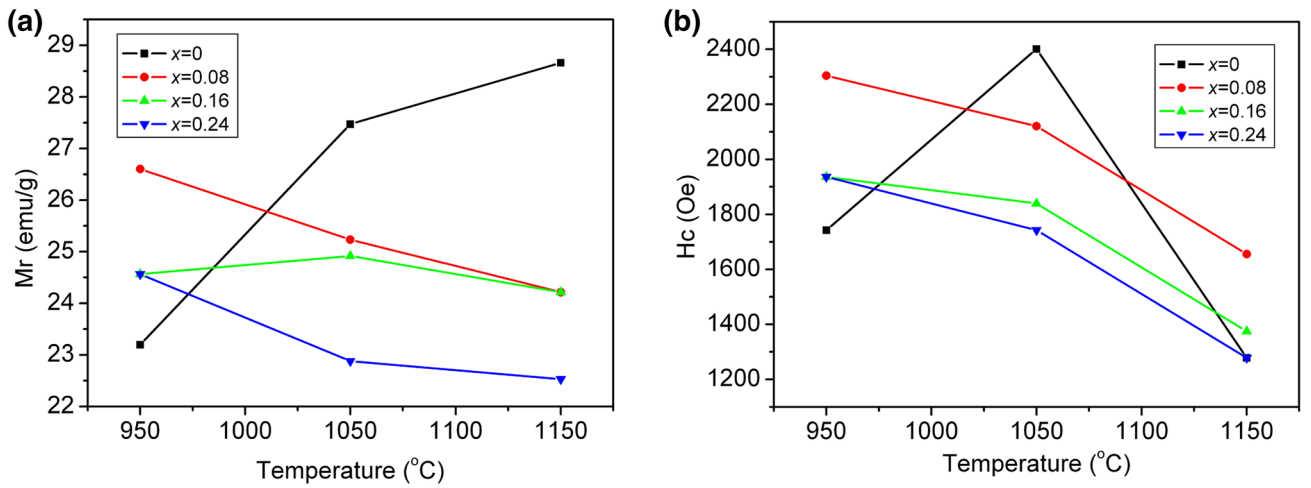

Fig. 9 Dependence of remanence (Mr) (**a**) and coercivity (Hc) (**b**) of $Ba_{0.5}Co_{0.5}Al_xFe_{12-x}O_{19}$ on substitution content (x) and calcination temperature

the crystallite size [25, 39]. The samples, calcined at 950 and 1050 °C, also has similar variation of coercivity as a function of the grain crystallite size. $Ba_{0.5}Co_{0.5}Fe_{12}O_{19}$, calcined at 1050 °C, has the highest coercivity value (2401.03 Oe); $Ba_{0.5}Co_{0.5}Fe_{12}O_{19}$ and $Ba_{0.5}Co_{0.5}Al_{0.24}Fe_{11.76}O_{19}$, calcined at 1150 °C, has the lowest coercivity value (1277.97 Oe). It has been reported earlier that a low value of coercivity is favorable for sensing application and is also one of the necessary conditions for electromagnetic (EM) materials [20, 40]. Therefore, hexagonal $Ba_{0.5}Co_{0.5}Al_xFe_{12-x}O_{19}$ is a kind of promising materials for sensing and electromagnetic applications.

Dependence of squareness ($R = Mr/Ms$) on calcination temperature and substitution content (x) is shown in Fig. 10a. Squareness (R) of $Ba_{0.5}Co_{0.5}Al_xFe_{12-x}O_{19}$ decreases with increase in calcination temperature except for $Ba_{0.5}Co_{0.5}Fe_{12}O_{19}$. The trend of squareness value of $Ba_{0.5}Co_{0.5}Al_xFe_{12-x}O_{19}$, calcined at 1050 and 1150 °C, decreases with the increase in substitution content (x). Squareness of $Ba_{0.5}Co_{0.5}Al_xFe_{12-x}O_{19}$ is 0.5113 for $x = 0$, 0.5018 for $x = 0.08$, 0.4810 for $x = 0.16$, and 0.4806 for $x = 0.24$, respectively. Correlation between magnetic domain type of ferrites and R values is as follows: Larger R values ($R \geq 0.5$) indicate that ferrite is in a single magnetic domain, and smaller R values ($R < 0.5$) are expected only in the case of the formation of a multi-domain structure [39]. Therefore, $Ba_{0.5}Co_{0.5}Al_xFe_{12-x}O_{19}$ ($x = 0.0$ and 0.08), calcined at 1150 °C, are of a single magnetic domain. $Ba_{0.5}Co_{0.5}Al_{0.16}Fe_{11.84}O_{19}$ and $Ba_{0.5}Co_{0.5}Al_{0.24}Fe_{11.76}O_{19}$ samples are of a multi-domain type.

The magnetic moment of $Ba_{0.5}Co_{0.5}Al_xFe_{12-x}O_{19}$ samples is estimated using the following relationship [41, 42]:

$$\eta_B = M \times Ms/5585, \tag{7}$$

where M is the molecular weight of the composition, and Ms is the specific saturation magnetization (emu/g), η_B is the magnetic moment (μ_B). The dependence of magnetic moment (η_B) on calcination temperature and substitution content (x) for $Ba_{0.5}Co_{0.5}Al_xFe_{12-x}O_{19}$ is shown in Fig. 10b. The magnetic moment of $Ba_{0.5}Co_{0.5}Fe_{12}O_{19}$ and $Ba_{0.5}Co_{0.5}Al_{0.16}Fe_{11.84}O_{19}$ increases with the increase in calcination temperature; that of $Ba_{0.5}Co_{0.5}Al_{0.08}Fe_{11.92}O_{19}$ slightly decreases with the increase in calcination temperature. By contrast, the magnetic moment of $Ba_{0.5}Co_{0.5}Al_{0.24}Fe_{11.76}O_{19}$ decreases with the increase in calcination temperature at first, then slightly increases at 1150 °C. Besides, the trend of the magnetic moment of $Ba_{0.5}Co_{0.5}Al_xFe_{12-x}O_{19}$ decreases with the increase in substitution content (x). $Ba_{0.5}Co_{0.5}Fe_{12}O_{19}$, calcined at 1150 °C, has the highest magnetic moment value (10.76 μ_B); $Ba_{0.5}Co_{0.5}Fe_{12}O_{19}$, calcined at 950 °C, has the lowest magnetic moment value (8.67 μ_B).

The effective anisotropy constant (K_{eff}) of $Ba_{0.5}Co_{0.5}Al_xFe_{12-x}O_{19}$ is calculated using Eq. (8) [34].

$$Hc = 0.985K_{eff}/Ms, \tag{8}$$

where Hc is the coercivity and Ms is the specific saturation magnetization. The results are shown in Fig. 11. The effective anisotropy constants (K_{eff}) of $Ba_{0.5}Co_{0.5}Al_xFe_{12-x}O_{19}$, calcined at 950 and 1150 °C, exhibit non-linear variation with substitution content (x). By contrast, the effective anisotropy constants (K_{eff}) of $Ba_{0.5}Co_{0.5}Al_xFe_{12-x}O_{19}$, calcined at 1050 °C, decrease with substitution content. The effective anisotropy constants (K_{eff}) of $Ba_{0.5}Co_{0.5}Al_xFe_{12-x}O_{19}$, calcined at 1050 °C, are 131725.3(0) erg/g for $x = 0$; 103170.0(7) erg/g for $x = 0.08$; 96322.0(8) erg/g for $x = 0.16$; and 81697.4(3) erg/g for $x = 0.24$, respectively.

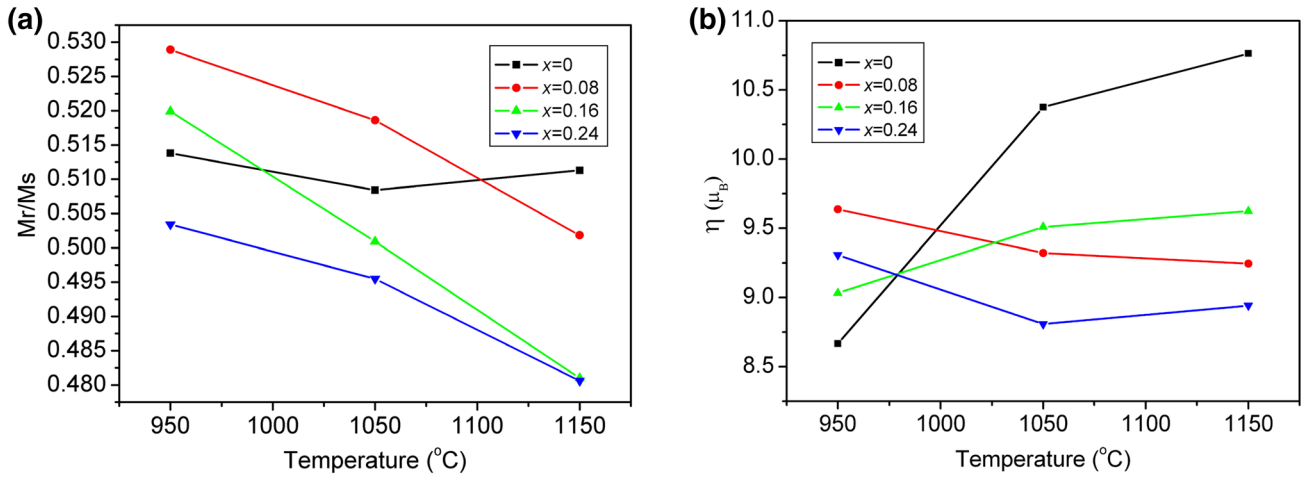

Fig. 10 Dependence of squareness (Mr/Ms) (**a**) and magnetic moment (η_B) (**b**) of $Ba_{0.5}Co_{0.5}Al_xFe_{12-x}O_{19}$ on substitution content (x) and calcination temperature

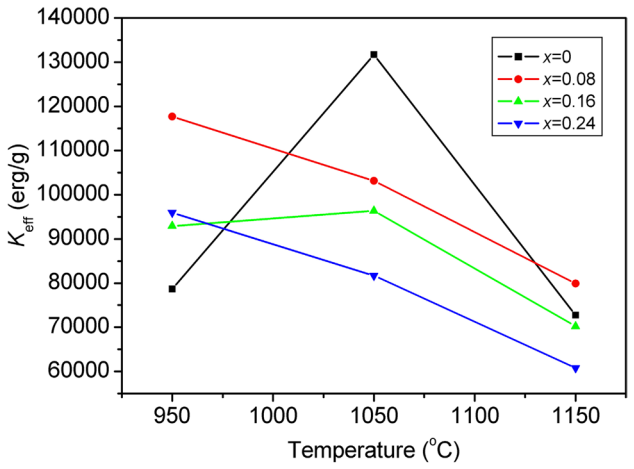

Fig. 11 Dependence of effective anisotropy constants (K_{eff}) of $Ba_{0.5}Co_{0.5}Al_xFe_{12-x}O_{19}$ on Al^{3+} content and calcination temperature

4 Conclusions

Al substituted M-type Ba-Co hexaferrite with composition $Ba_{0.5}Co_{0.5}Al_xFe_{12-x}O_{19}$ ($x=0$, 0.08, 0.16, and 0.24) was successfully synthesized by the ball-milling assisted ceramic process. XRD and SEM analysis confirm the formation of M-type Ba-Co hexaferrite with platelet-like morphology when $Ba_{0.5}Co_{0.5}Al_xFe_{12-x}O_{19}$ ($x=0$, 0.08, 0.16, and 0.24) precursors are calcined at 950 °C in air for 3 h. Lattice parameters "*a*" and "*c*" values of $Ba_{0.5}Co_{0.5}Al_xFe_{12-x}O_{19}$ decrease with the increase in substitution content (x). Average crystallite size of $Ba_{0.5}Co_{0.5}Al_xFe_{12-x}O_{19}$ sample, calcined at 1150 °C, decreases obviously after substituting Fe^{3+} ions by Al^{3+} ions. The is because the bond energy of Al^{3+}–O^{2-} is much larger than that of Fe^{3+}–O^{2-}. Magnetic characterization indicates that substitution of Fe^{3+} ions by Al^{3+} ions can improve the specific saturation magnetizations and coercivity when $Ba_{0.5}Co_{0.5}Al_xFe_{12-x}O_{19}$ precursors are calcined at 950 °C. However, when $Ba_{0.5}Co_{0.5}Al_xFe_{12-x}O_{19}$ precursors are calcined at 1050 and 1150 °C, specific saturation magnetization of Al-substituted samples decreases with the increase in substitution content (x). $Ba_{0.5}Co_{0.5}Fe_{12}O_{19}$, calcined at 1150 °C, has the highest specific saturation magnetization value (56.07 emu/g), remanence (28.66 emu/g), and moment (10.76 μ_B); $Ba_{0.5}Co_{0.5}Fe_{12}O_{19}$, calcined at 1050 °C, has the highest coercivity value (2401.03 Oe) and effective anisotropy constants (131725.30 erg/g). With the increase of doping content (x), magnetic domain type of ferrites, calcined at 1050 and 1150 °C, changes from a single magnetic domain to a multi-domain type. Based on a low value of coercivity, hexagonal $Ba_{0.5}Co_{0.5}Al_xFe_{12-x}O_{19}$ is a kind of promising material for sensing and electromagnetic applications.

Acknowledgements This study was financially supported by the National Natural Science Foundation of China (Grant No. 21603040) and the Guangxi Natural Science Foundation of China (Grant Nos. 2016GXNSFDA380034, 2016GXNSFBA380062).

References

1. A. Gonzalez-Angeles, A. Gruskova, J. Lipka, J. Slama, V. Jancarik, J. Phys. **1**, 37–42 (2008)
2. M. Cernea, S.G. Sandu, C. Galassi, R. Radu, V. Kuncser, J. Alloys Compd. **561**, 121–128 (2013)
3. H.F. Yu, J. Magn. Magn. Mater. **341**, 79–85 (2013)
4. R.C. Pullar, Prog. Mater. Sci. **57**, 1191–1334 (2012)
5. J. Krishna Murthy, C. Mitra, S. Ram, A. Venimadhav, J. Alloys Compd. **545**, 225–230 (2012)
6. R. Nowosielski, R. Babilas, J. Wrona, J. Achieve, Mater. Manuf. Eng. **20**, 307–310 (2007)
7. Y.W. Li, Q. Wang, H. Yang, Curr. Appl. Phys. **9**, 1375–1380 (2009)
8. H. Sözeri, İ Küçük, H. Özkan, J. Magn. Magn. Mater. **323**, 1799–1804 (2011)
9. V.C. Chavan, S.E. Shirsath, M.L. Mane, R.H. Kadam, S.S. More, J. Magn. Magn. Mater. **398**, 32–37 (2016)
10. S.F. Kong, P.P. Zhang, X.F. Wen, P.H. Pi, J. Cheng, Z.R. Yang, J. Hai, Particuology **6**, 185–190 (2008)
11. G. Murtaza Rai, M.A. Iqbal, K.T. Kubra, J. Alloy. Compd. **495**, 229–233 (2010)
12. Z. Mosleh, P. Kameli, A. Poorbaferani, M. Ranjbar, H. Salamati, J. Magn. Magn. Mater. **397**, 101–107 (2016)
13. S. Ounnunkad, Solid State Commun. **138**, 472–475 (2006)
14. L.X. Wang, Q. Huang, L. Mu, Q.T. Zhang, J. Rare Earths. **25**(Suppl), 216–219 (2007)
15. V. Anbarasu, P.M. Md Gazzali, T. Karthik, A. Manigandan, K. Sivakumar, J. Mater. Sci.: Mater. Electron. **24**, 916–926 (2013)
16. W. Chen, W.W. Wu, M.M. Mao, C. Zhou, S.F. Zhou, M.Y. Li, Q. Wang, J. Supercond. Nov. Magn. **30**, 707–714 (2017)
17. G.B. Teh, S. Nagalingam, D.A. Jefferson, Mater. Chem. Phys. **101**, 158–162 (2007)
18. V.N. Dhage, M.L. Mane, A.P. Keche, C.T. Birajdar, K.M. Jadhav, Phys. B. **406**, 789–793 (2011)
19. M.A. Rafiq, M. Waqar, T.A. Mirza, A. Farooq, A. Zulfiqar, J. Electron. Mater. **46**, 241–246 (2017)
20. W. Abbas, I. Ahmad, M. Kanwal, G. Murtaza, I. Ali, M.A. Khan, M.N. Akhtar, M. Ahmad, J. Magn. Magn. Mater. **374**, 187–191 (2015)
21. Y. Liu, M.G.B. Drew, Y. Liu, J.P. Wang, M.L. Zhang, J. Magn. Magn. Mater. **322**, 814–818 (2010)
22. J. Singh, C. Singh, D. Kaur, S. Bindra Narang, R. Joshi, S.R. Mishra, R. Jotania, M. Ghimire, C.C. Chauhan, Mater. Des. **110**, 749–761 (2016)
23. R.S. Alam, M. Moradi, M. Rostami, H. Nikmanesh, R. Moayedi, Y. Bai, J. Magn. Magn. Mater. **381**, 1–9 (2015)
24. J.P. Wang, C.L. Wu, T. Xia, Y. Liu, J. Feng, M.L. Zhang, J. Wuhan Univ. Technol.-Mater. Sci. Ed. **27**, 507–511 (2012)
25. K.W. Zhou, W. Chen, X.H. Wu, W.W. Wu, C.W. Lin, J. Wu, J. Electron. Mater. **46**, 4618–4626 (2017)
26. C.C. Liu, X.S. Liu, S.J. Feng, K.M. Ur Rehman, M.L. Li, C. Zhang, H.H. Li, X.Y. Meng, J. Magn. Magn. Mater. **436**, 126–129 (2017)
27. X.H. Wu, W. Chen, W.W. Wu, Y.Y. Chen, T.W. Li, C.Y. Zhang, H.X. Zhang, J. Mater. Sci. **52**, 10085–10097 (2017)
28. W. Chen, W.W. Wu, X.H. Wu, T.W. Li, J. Wu, H.X. Zhang, J. Mater. Sci.: Mater. Electron. **28**, 7874–7883 (2017)

29. D.M. Chen, I. Harward, J. Baptist, S. Goldman, Z. Celinski, J. Magn. Magn. Mater. **395**, 350–353 (2015)
30. H.Z. Wang, B. Yao, Y. Xu, Q. He, G.H. Wen, S.W. Long, J. Fan, G.D. Li, L. Shan, B. Liu, L.N. Jiang, L.L. Gao, J. Alloys Compd. **537**, 43–49 (2012)
31. Y.L. Chai, Y.S. Chang, G.J. Chen, Y.J. Hsiao, Mater. Res. Bull. **43**, 1066–1073 (2008)
32. X.Z. Guo, H. Yang, M. Cao, C. Han, F.F. Song, Trans. Nonferrous Met. Soc. China. **16**, 593–597 (2006)
33. Y. Zhou, X.H. Wu, W.W. Wu, Ch Wen, Q. Wang, J. Supercond. Nov. Magn. J. Supercond. Nov. Magn. **31**, 521–528 (2018)
34. X.H. Wu, W. Chen, W.W. Wu, H.J. Li, C.W. Lin, J. Electron. Mater. **46**, 199–207 (2017)
35. S.M. El-Sayed, T.M. Meaz, M.A. Amer, H.A.E.I. Shersaby, Phys. B. **426**, 137–143 (2013)
36. G. Ramezanzaeh, A. Ghasemi, R. Mozaffarinia, A. Alizadeh, Ceram. Int. **43**, 10231–10238 (2017)
37. C.J. Li, B.N. Huang, J.N. Wang, J. Mater. Sci. **48**, 1702–1710 (2013)
38. Y.J. Yang, F.H. Wang, X.S. Liu, J.X. Shao, D.H. Huang, J. Magn. Magn. Mater. **421**, 349–354 (2017)
39. X.H. Wu, W. Chen, W.W. Wu, Yu Ning, S.S. Chen, J. Mater. Sci.: Mater. Electron. **28**, 18815–18824 (2017)
40. M. Ahmad, R. Grössinger, M. Kriegisch, F. Kubel, M.U. Rana, Curr. Appl. Phys. **12**, 1413–1420 (2012)
41. W. Chen, W.W. Wu, D.S. Liu, J. Wu, J. Mater. Sci.: Mater. Electron. **28**, 2901–2909 (2017)
42. X.H. Wu, W. Chen, W.W. Wu, J. Wu, Q. Wang, J. Magn. Magn. Mater. **453**, 246–253 (2018)